JOURNAL OF GEOPHYSICAL RESEARCH, VOL. 106, NO. D7, PAGES 7399–7414, APRIL 16, 2001

OH radicals in the boundary layer of the Atlantic Ocean 1. Measurements by long-path laser absorption spectroscopy

Theo Brauers, Martin Hausmann,[1] Arne Bister,[2] Alexander Kraus,[3] and Hans-Peter Dorn
Institut für Atmosphärische Chemie, Forschungszentrum Jülich, Jülich, Germany.

Abstract. Knowing the concentration of hydroxyl (OH) radicals is most important for the understanding of the chemical processes in the troposphere. This paper describes the first direct measurements of OH in the boundary layer of the tropical Atlantic Ocean. The use of Differential Optical Absorption Spectroscopy provided direct measurements of OH with a calibration uncertainty of 6%. The 1-σ precision of the OH data was in the range of $(1\text{–}4)\times10^6$ cm^{-3} because of the exceptional experimental conditions encountered on the ship. On 10 measurement days we collected a total of 483 OH concentration data between 5°N and 40°S. Careful analysis was applied to select data not affected by the ship and its exhaust. The selected data ($N = 238$) exhibit diurnal profiles with maxima around 7×10^6 cm^{-3} for overhead Sun and clean air conditions. On average the measured OH concentrations are 16% higher than corresponding box model calculations based on simultaneously measured trace gas concentrations and photolysis frequencies. The deviation from the 1:1 relation, however, is covered by the combined calibration errors of OH, CO, and the photolysis frequencies.

1. Introduction

OH radicals are known to play an important role in the troposphere [e.g., *Logan et al.*, 1981; *Ehhalt et al.*, 1991; *Thompson*, 1992]. OH reacts with a wide variety of gaseous species initiating their degradation. For CO and most hydrocarbons the reaction with OH is the rate- limiting step determining their residence time in the troposphere. OH is primarily produced by the UV photolysis ($\lambda < 345$ nm) of ozone to excited O(^1D) atoms (please note that reaction numbers refer to those of Table 3):

$$O_3 + h\nu \rightarrow O_2 + O(^1D)$$

(reaction (R1)). $J(O^1D)$ is the photolysis frequency related to this process. About 10–20% of the O(^1D) atoms react with water vapor, forming OH radicals,

$$H_2O + O(^1D) \rightarrow 2\,OH$$

(reaction (R2)), while the remainder is quenched by collisions with N_2 and O_2. Another, but in general minor, primary source is the photolysis of H_2O_2:

$$H_2O_2 + h\nu \rightarrow 2\,OH$$

(reaction (R5)). A secondary source of OH is the reaction of NO or ozone with HO_2 radicals,

$$HO_2 + NO \rightarrow NO_2 + OH$$

$$HO_2 + O_3 \rightarrow 2\,O_2 + OH$$

(reactions (R6) and (R7), respectively), which are produced during the photolysis of HCHO and during the oxidation of CO,

$$OH + CO\,(+O_2) \rightarrow CO_2 + HO_2$$

(reaction (R8)), and other reduced species like methane, hydrocarbons, SO_2, and formaldehyde. However, under clean air conditions with low NO_X ($= NO + NO_2$) the primary formation of OH via ozone photolysis dominates. The reactions R6 – R8 couple OH and HO_2 to the HO_X ($= OH + HO_2$) cycle. The sinks of HO_X radicals are the reactions of OH with NO_2 forming HNO_3 and the reactions of the HO_2 and RO_2 radicals forming peroxides. Again, under low NO_X conditions the formation of HNO_3 is a minor contribution to the overall HO_X loss.

[1]Now at Hoffmann Meßtechnik GmbH, Dielheim, Germany
[2]Now at Rational Software GmbH, Düsseldorf, Germany
[3]Now at Grünenthal GmbH, Aachen, Germany

Paper number 2000JD900679.
0148-0227/01/2000JD900679$09.00

Although a number of experimental photochemistry studies have been performed in the marine boundary layer (MBL) above the tropical oceans, OH concentrations have never been measured directly. Published OH concentrations in the MBL are based on models taking into account solar radiation and trace gas measurements. For the conditions during the ANT VII/1 expedition of R/V *Polarstern* in 1988 on the Atlantic Ocean, *Platt et al.* [1992] estimated peak OH concentrations of $7\times10^6\,cm^{-3}$ from measured data of photolysis frequencies and trace gas concentrations. *Thompson et al.* [1993] analyzed the ozone observations and photochemistry during the SAGA-3 experiment by using a one-dimensional model. On the basis of observations in the equatorial Pacific, they reported a diurnally averaged OH of $8.9\times10^5\,cm^{-3}$ and peak levels of $4\times10^6\,cm^{-3}$ at 9 ppb of ozone. *Cooper* [1996] analyzed the levels and diurnal cycles of dimethyl sulfide (DMS) from a number of studies and estimated OH 24-hour averages of $1.6\times10^6\,cm^{-3}$ for the tropical Pacific and between $1.8\times10^6\,cm^{-3}$ and $2.9\times10^6\,cm^{-3}$ for the tropical Atlantic. These and other indirect determinations are based on assumptions about the photochemistry, and they show the need for direct insitu OH measurements simultaneously with its precursors and reaction partners.

Measuring tropospheric OH is still demanding and costly. In the last decades a number of techniques to measure the local OH concentration were developed and explored in atmospheric chemistry field campaigns (see *Crosley* [1995] and other contributions to the special issue of the *Journal of Atmospheric Sciences* for an overview of the methods and instruments being available through 1994). The most sensitive OH detection techniques today are Laser-Induced Fluorescence (LIF) [e.g., *Holland et al.*, 1998] and Ion-Assisted Mass Spectrometry (IAMS) [e.g., *Tanner et al.*, 1997], which were shown to detect OH in the 10^5 molecules/cm^3 range over an averaging time of 60 s or less.

Long-path Differential Optical Absorption Spectroscopy (DOAS), however, is the only technique which requires neither chemical transformation of OH (like IAMS) nor in-field calibration of the instrument (like LIF and IAMS). The OH concentration measured by DOAS is basically calculated from Beer's law:

$$D' = \ln(I'_0/I) = \sigma' \times L \times [\mathrm{OH}] \quad , \qquad (1)$$

where D' is the differential optical density. D' is calculated from the measured intensity I and I'_0. For several OH absorption lines around 308 nm the effective differential absorption cross section, σ', is high enough to achieve measurable optical densities at reasonable light path lengths L (a few kilometers) and typical daytime OH concentrations. In the case of OH the absorption cross section can be calculated with only 6% uncertainty from well-known molecular properties, temperature, pressure, and the spectral resolution of the instrument [*Dorn et al.*, 1995].

The OH DOAS technique was pioneered by *Perner et al.* [1976], and in the following years a number of field campaigns with DOAS instruments have been realized (Table 1). The complex setup of all OH DOAS instruments did limit their application to ground-based measurements, and most of the measurements were performed at the site of the respective laboratory [*Eisele et al.*, 1994; *Mount et al.*, 1997a; *Callies*, 1988]. In addition, it was realized from the early measurements of OH radicals that spatially integrated concentrations over several kilometers of extended light path made it difficult to compare DOAS with other techniques [*Eisele et al.*, 1994; *Mount et al.*, 1997b] and models [*Poppe et al.*, 1994; *McKeen et al.*, 1997]. This problem was solved with the application of multireflection cells in DOAS OH experiments [*Gerlach*, 1991; *Armerding et al.*, 1992; *Dorn et al.*, 1995]. These cells allow the realization of light paths of the order of several kilometers within an optical cell length of 10–40 m even under rough field conditions and on mobile platforms.

Table 1. Application of DOAS Instruments for OH Measurements in Field Campaigns.

Campaign	Time	Location	Light Path	Detection Limit[a]	Reference[b]
Jülich	1980	51°N, 6°E	5.6 km (2×2.7 km)	≈ 2	1
Schauinsland	June 1984	51°N, 6°E	8.6 km (1×8.6 km)	≈ 3	2
Jülich	May 1988 / May1987	51°N, 6°E	5.6 km (2×2.7 km)		3
Fritz Peak	1991	40°N, 105°W	20.6 km (2×10.3 km)		4
TOHPE	Aug.-Sep. 1993	40°N, 105°W	20.6 km (2×10.3 km)	0.8–1.5	5
Teneriffe	May 1994	28°N, 16°W	1.2 km (200×6.0 m)	0.8	6
POPCORN	Aug. 1994	54°N, 12°E	1.848 km (48×38.5 m)	1.7	7
ALBATROSS[c]	Oct-Nov 96	5°N–37°S 26°–36°W	2.21 km (112×19.74 m)		this work

[a]Detection limit (2σ) in 10^6 molecules/cm^3

[b]References: 1, *Hübler et al.* [1984]; 2, *Platt et al.* [1988]; 3, *Poppe et al.* [1994]; 4, *Eisele et al.* [1994]; 5, *Mount et al.* [1997a] 6, *Armerding et al.* [1997]; 7: *Brandenburger et al.* [1998]

[c]This experiment, Air Chemistry and Lidar Studies of Tropospheric and Stratospheric Species on the Atlantic Ocean (ALBATROSS). See discussion about detection limit in Sect. 2.2

In this paper, we present the first OH measurements recorded in the tropical marine boundary layer with a DOAS instrument. Our instrument including the multireflection cell was operated aboard ship for the first time. The measurements were carried out aboard the R/V *Polarstern* during the Air Chemistry and Lidar Studies of Tropospheric and Stratospheric Species on the Atlantic Ocean (ALBATROSS) campaign and this paper will emphasize OH concentration measurements and data analysis considering the special experimental conditions encountered. This paper also presents additional data, for example, meteorological parameters, photolysis frequencies, and the concentrations of trace gases, in order to support the interpretation of the measured OH data by model calculations.

2. Experiment

2.1. Instrument

Our long-path DOAS OH experiment has been described in detail [*Dorn et al.*, 1995; *Hausmann et al.*, 1997], and we will give only a brief description here. The instrument measures the UV absorption of individual rotational transitions in the A–X electronic system of the OH radical. We simultaneously observe a spectral range of 0.22 nm centered at 308.1 nm which comprises six OH lines, namely, $Q_1(2)$, $Q_{21}(2)$, $R_2(2)$, $Q_1(3)$, $Q_{21}(2)$, and $P_1(1)$. The instrument consists of three major parts: a broadband laser light source, a multireflection cell (MRC), and a high-resolution spectrograph. While the laser and the spectrograph were setup on an optical table in a sea container, the MRC was located outside in the atmosphere.

The laser is a mode-locked picosecond frequency-doubled dye laser providing a broadband ("white") light source of 0.42 nm full width at half maximum centered at 308.1 nm. During the cruise we faced the problem of strong vibrations of the ship which introduced variability in the intensity distribution of the laser output. Therefore we sporadically controlled the laser spectrum of the dye laser by means of an auto-correlator under different conditions during the cruise [*Bister*, 1997]. We did not find any evidence for fluctuations of the laser pulse duration which would lead to stochastic modulations of the laser output spectrum affecting the precision of the OH detection.

The open multireflection cell is a modified White cell [*Hausmann et al.*, 1997] set to a base length of 19.74 m. On the ship we could achieve a light path length of 2211 m corresponding to 112 travels of the laser beam through the MRC. The spectrograph (Sopra F1500) used was identical to the one used during the Photo-Oxidant Formation by Plant Emitted Compounds and OH Radicals in North-Eastern Germany (POPCORN) field campaign [*Brandenburger et al.*, 1998] allowing the simultaneous recording of a spectral range of 0.22 nm using a photodiode array detector (Princeton Instruments, ST 1015).

2.2. Spectra Recording and Data Analysis

The spectra recording and data analysis were a major challenge during the ALBATROSS campaign. During the experiments we identified two sources of problems: First, the vibrations caused by the ship's engines and propellers propagated into the experimental setup. Although we used a vibration damping system for the entire optical setup, inside the container the spectrograph and laser were excited to weak vibrations which have affected the spectral resolution and laser alignment. Second, and more seriously, pitch and roll of the ship changed the wavelength setting of the spectrograph during the measurements. With these experimental difficulties aboard a ship, we had to introduce a number of new steps into the process of spectra gathering and evaluation. Therefore, we describe this process in some detail and we point out the difference to the evaluation of the OH measurements in Jülich 1993 and during the POPCORN field campaign in 1994 [*Brauers et al.*, 1995; *Dorn et al.*, 1995; *Hausmann et al.*, 1997; *Brandenburger et al.*, 1998; *Hausmann et al.*, 1999].

2.2.1. Spectra recording. The measurement of OH using DOAS requires an instrument sensitivity in the 10^{-5} optical density range. Since photodiode arrays consist of discrete pixels with individual light sensitivities, it is necessary to carefully determine the sensitivity pattern of the detector. In 1993, we introduced the multichannel scanning technique (MCST) (for details see *Brauers et al.* [1995]) which allowed the simultaneous measurement of absorption signal and pixel sensitivity by scanning the spectrograph during the recording of a set of diode array readouts. In previous measurements we recorded 100 readouts, each corresponding to 1-s integration time separated by a spectral shift of about 0.2 pm.

During the ALBATROSS campaign the wavelength setting of the high-resolution spectrograph kept wandering because pitch and roll of the ship caused a tilt of the grating. Typically, the center wavelength of the spectrograph changed by ±3 pm, corresponding to twice the linewidth of a OH line through one cycle of pitch or roll (≈5 s) of the ship. In order to monitor this unwanted turn of the spectrograph's grating during the OH measurements, we sent a HeNe laser beam into the spectrograph through an additional slit to illuminate the grating in such a way that a narrowband wavelength marker line was created in the center between the OH absorption lines at about 308.081 nm. We also increased the readout rate of the detector from 1 Hz to 10 Hz and saved every readout of the detector to disk. For one air spectrum we recorded 1500 readouts in blocks of 50 readouts at 30 different nominal wavelength settings of the spectrograph separated by a 0.7-pm increment, thus covering the same range as during POPCORN.

2.2.2. Conversion of raw data to absorption spectra. In a first step the set of 1500 readouts were added up according to the MCST in order to create a pixel-to-pixel reference of the photodiode array detec-

tor (for details, see *Brauers et al.* [1995]). Next, each of the readouts was divided by this pixel-to-pixel reference spectrum. In the following step the peak position of the HeNe line was searched and each readout was shifted accordingly to a common wavelength position. These spectra were finally added up to produce one air spectrum which, after band-pass filtering, were analyzed for atmospheric absorptions.

2.2.3. Air spectra to optical density, determination of measurement precision. The air spectra were analyzed by a least-squares (LS) fit of five reference spectra of OH, naphthalene ($C_{10}H_8$), SO_2, HCHO, and an unknown absorber X (Figure 1). Because the content of a single pixel of the resulting air spectrum after the application of the MCST is generally not independent of the content of adjacent pixels, the errors of the parameters as obtained from the LS fit are too small to represent the true measurement precision (for details, see *Hausmann et al.* [1997]). Therefore the calculation of the statistical errors was based on the procedure developed for the POPCORN data [*Hausmann et al.*, 1997; *Brandenburger et al.*, 1998; *Hausmann et al.*, 1999]. However, the conditions during this study were substantially different, since the spectral position was defined by the HeNe laser at pixel positions 480–580 in the raw data. We found that after application of the modified MCST the spectral position is already well defined; so the shift range during the fit of the reference spectra was reduced to ±2 pixels compared with the previous experiments where the reference spectra were allowed to be shifted by ±10 pixels.

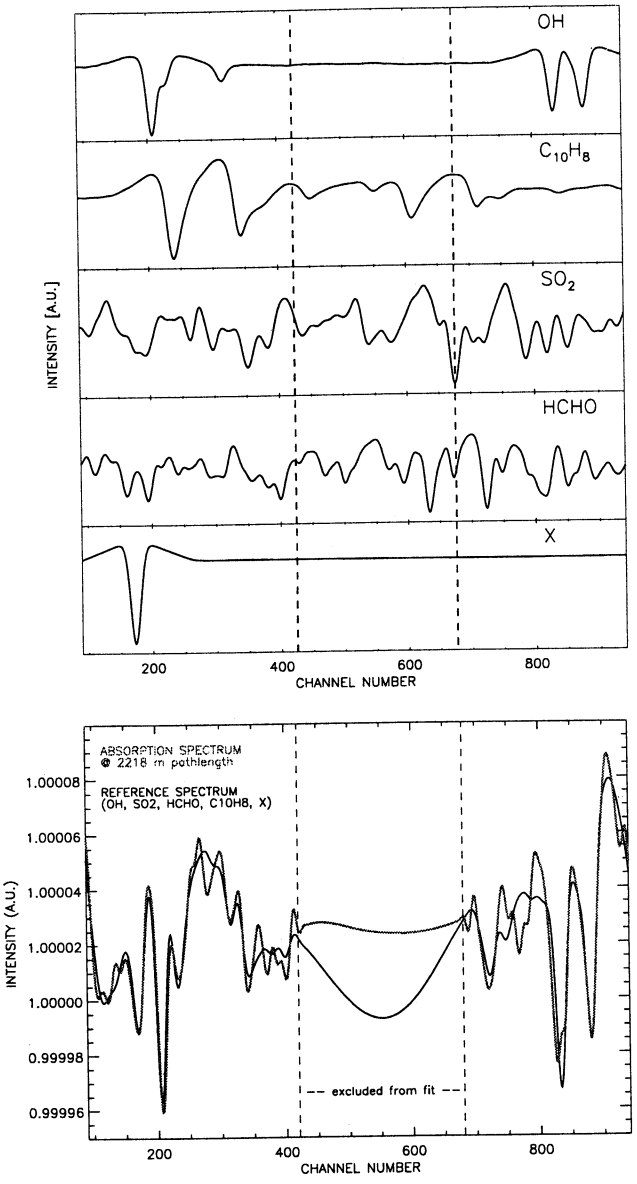

Figure 1. (top) Reference spectra of OH, naphthalene, SO_2, HCHO, and the unknown absorber X. The spectra correspond to a spectral resolution of 2.6 pm. (bottom) Example of the analysis of a spectrum recorded during the cruise. The range between pixels 420 and 680 was excluded from the analysis since this range was covered by the HeNe reference line which was used for the online monitoring of the actual wavelength setting of the spectrograph.

Table 2. Effective Differential Absorption Cross Sections for the Selected Lines of OH, HCHO, SO_2, and $C_{10}H_8$.[a]

Species	λ, nm	σ, cm^2
OH	307.9951	8.78×10^{-17}
HCHO	308.0020	4.95×10^{-21}
SO_2	308.1145	1.42×10^{-20}
$C_{10}H_8$	308.1034	5.65×10^{-19}

[a]These cross sections are smaller than those used during the POPCORN field campaign with the same instrument [*Brandenburger et al.*, 1998]. This is due to the reduced spectral resolution on the ship.

Compared with the precision of POPCORN OH data (see Figure 4 of *Brandenburger et al.* [1998]), the statistical errors of the ALBATROSS measurements are about a factor of 2 higher (see Figure 5). This is mainly caused by the movement of the ship, resulting in a lower light intensity recorded during each cycle of 1500 readouts. Also, the spectral intervals containing the HeNe marker was not available for the LS fit of the reference spectra (Figure 1), thus decreasing the measurement precision considerably.

2.2.4. Optical density to concentration conversion (measurement accuracy). The fit procedure gives the differential optical density of a certain absorption line. This value was then converted to a concentration by using equation 1 with the light path which is easily calculated from the number of travels in the multireflection cell (error of $< 5\%$ [*Hausmann et al.*, 1997]) and the effective cross sections listed in Table 2. Since the spectral resolution is slightly altered by the procedure used on the ship when compared with the POPCORN campaign [*Hausmann et al.*, 1997], the effective cross sections (Table 2) are slightly lower than those used during POPCORN [*Brandenburger et al.*,

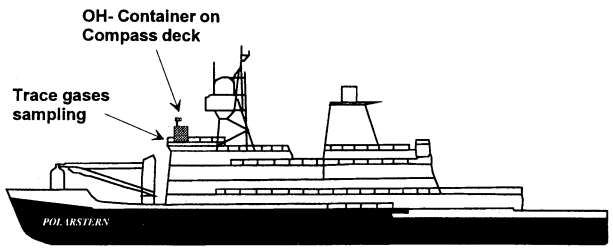

Figure 2. Side view of the R/V *Polarstern*. The OH experiments were installed on the compass deck above the bridge. The inlets of the sampling lines for O_3, CO, CH_4, HCHO, H_2O_2, and NO_X were at the altitude of the rail. The compass deck is about 25 m above the sea surface.

1998]. Nevertheless, the accuracy of the cross section used here is again about 6%, as for the previous experiment.

2.3. Setup Aboard the Ship

The DOAS instrument (laser and spectrograph) was housed in an air-conditioned 20-feet container on the compass deck of R/V *Polarstern* at a height of 25 m above the sea surface. Figure 2 shows R/V *Polarstern* from port side with the location of the instruments. Provided there is a relative wind component from the bow, the compass deck is the premier location for sampling unpolluted air. Figure 3 shows a schematic of the compass deck of the R/V *Polarstern* from top and the layout of the instrumental setup. The DOAS container was located on the starboard side. An aluminum box, which housed the mirrors and prisms of the field mirror side of the White cell, was installed on top of the container. This box was attached to a steel frame on the container roof providing a height of 1.5 m above the container roof. On top of another container at the port side (housing the laser induced fluorescence instrument) the camera mirrors of the White cell were mounted in a similar box. The light was traveling parallel to the surface of the compass deck at an altitude of 4.1 m above the deck's surface corresponding to 29 m above sea level.

2.4. Additional Measurements

Most other insitu instruments were also installe on the compass deck. The data of these instruments were used as input parameters for our model calculation as well as for the identification and exclusion of those OH measurements which were influenced by the ship's exhaust. Ultrasonic anemometers (Metek, USA-1) were operated at two locations (Figure 2) to record the local relative wind velocities at 1-min time resolution. Simultaneously, we monitored temperature and humidity with standard meteorological equipment. We also recorded the ozone mixing ratios with two UV absorption instruments (DASIBI 1003, Ansyco) sampling air from the port side and the starboard side of the compass deck.

Photolysis frequency measurements during ALBATROSS were performed by using actinic flux spectroradiometry [cf. *Kraus and Hofzumahaus*, 1998]. Photolysis frequencies are some of the most important input parameters for model calculations and thus were measured with high precision. A double-monochromator spectrometer, equipped with a collecting entrance optics showing nearly uniform spatial sensitivity over 2π sr field of view is calibrated radiometrically in terms of absolute actinic photon fluxes $F_\lambda(\lambda)$ (photons cm^{-2} nm^{-1} s^{-1}). The spectrometer was installed inside the temperature regulated LIF container (see Figure 3). The optical inlet was mounted on a 2-m mast on top of the container and was coupled to the spectrometer by a 5-m quartz fiber bundle. Spectra of $F_\lambda(\lambda)$ in the range of 280 nm to 420 nm were recorded with a spectral bandwidth and incremental step size of 1 nm. The time resolution for the measurement of a single spectrum was about 70 s. Details of the instrumental setup of the spectroradiometer and the method of calibration for the actinic flux measurement is given by *Hofzumahaus et al.* [1999]. From the measured spectra of the actinic flux $F_\lambda(\lambda)$ the photolysis frequencies $J(i)$ of the various molecules i were calculated using

$$J(i) = \int \sigma_i(\lambda) \cdot \phi_i(\lambda) \cdot F_\lambda(\lambda)\, d\lambda \qquad (2)$$

where the absorption cross sections $\sigma_i(\lambda)$ and the molecular quantum yield $\phi_i(\lambda)$ were taken from the literature as described by *Kraus and Hofzumahaus* [1998].

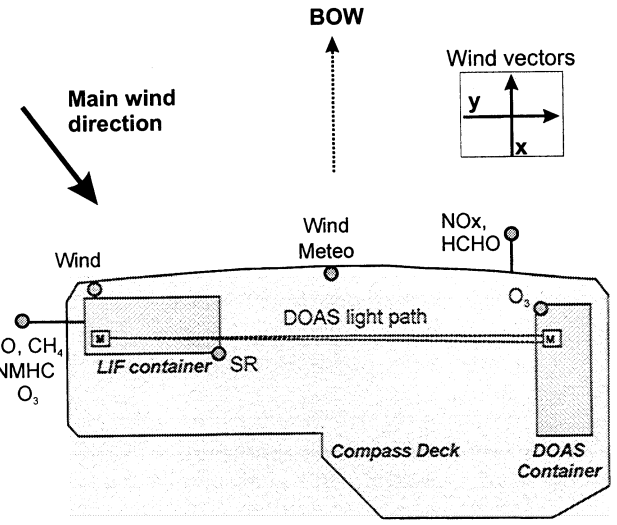

Figure 3. Setup of the experiment on the compass deck of the R/V *Polarstern*: CO, CH_4, NMHC, and O_3, location of the inlet; wind, ultrasonic anemometer; SR, spectroradiometer; wind and meteo: ultrasonic anemometer and meteorological parameters; NO_X and HCHO, inlet for measurement of NO, NO_X, HCHO, and H_2O_2; O_3, second inlet for ozone measurements on starboard side; The light path of 19.72 m of the DOAS experiment between the mirrors (M) was 4 m above the deck.

Different from their publication, the quantum yield for the $O(^1D)$ formation from O_3 photolysis was calculated according to the temperature dependent parameterizations given in the most recent publication by *Talukdar et al.* [1998]. The ozone absorption cross section was taken from *Daumont et al.* [1992]. The absorption cross section of NO_2 used to calculate $J(NO_2)$ was from *Merienne et al.* [1995]. The cross-section data for the determination of the methylhydroperoxide photolysis frequency $J(CH_3O_2H)$ was measured by *Vaghjiani and Ravishankara* [1989], and the quantum yield for the formation of $CH_3O + OH$ was assumed to be unity. The total systematic uncertainties of the resulting photolysis frequencies, including the error of the actinic flux measurements and the uncertainties in the molecular photodissociation data, are estimated to be ±15% for $J(O^1D)$ and $J(NO_2)$. For the uncertainties of the other photolysis frequencies, see the discussion of *Kraus and Hofzumahaus* [1998].

M. Gautrois et al. (unpublished data) measured CO, methane, and nonmethane hydrocarbons (NMHC) on the port side of the compass deck side by side with one of our ozone inlets. *Weller et al.* [2000] measured NO, NO_X, and HCHO by using an inlet tubing on the top of the rail of the compass deck just in front of the DOAS container. *Weller et al.* [2000] also measured H_2O_2 and CH_3O_2H by using a short inlet line at 15 m above sea level on the starboard side.

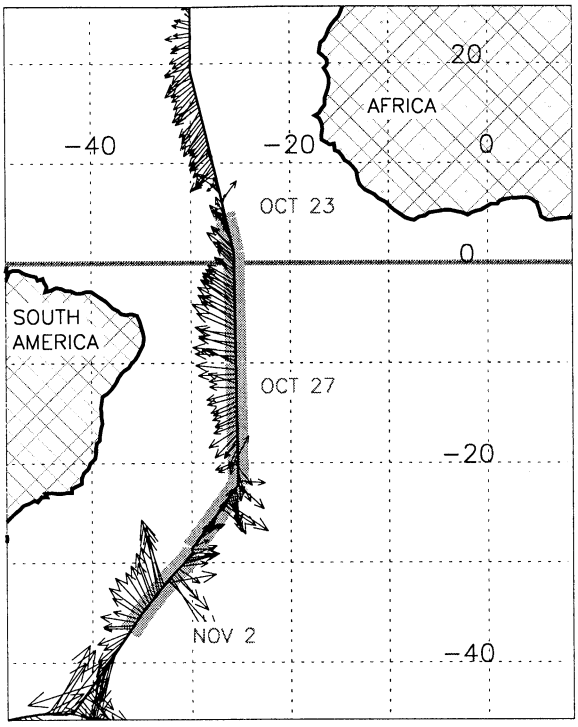

Figure 4. Map shows part of the route of the R/V *Polarstern* from Bremerhaven, Germany, to Punta Aquilla, Argentina. The thick grey line of track indicates the part of the cruise where DOAS OH data were recorded (October 23 to November 2, 1996). The arrows correspond to the 1-hour average wind speed and direction measured at the ship's location.

3. Results and Discussion

3.1. Results and Selection of Data

The cruise ANT XIV/1 of the R/V *Polarstern* (October 5 to Novemebr 10) covered a latitudinal range from 68°N to 50°S. Our measurements, however, were restricted to a leg of the cruise from October 23 to November 2 (Figure 4) because of heavy weather in the northern part of the Atlantic and the technical problems described above.

A total of 492 OH measurements were recorded on 10 measurement days (Plate 1). During this period we went from the tropical ocean just south of Intertropical Convergence Zone (5°N) to the southern westwind zone at 40°S. The OH data set shows diurnal profiles with maxima at local noon around 7×10^6 cm^{-3} and peaks of 2×10^7 cm^{-3} on October 29. A series of high OH values especially on October 29 may be indicative of local trace gas emissions specific to the ship. In order to examine possible influences of local emissions on the measured OH data, we analyzed all data with respect to the pollution indicators CO, ozone, and NO_X and the relative wind speed.

The relative wind velocity components u_X (stern to bow) and u_Y (port side to starboard side; see Figure 3)

Plate 1. Measured time series of OH concentration, CO, ozone, NO, and NO_X mixing ratios, wind velocities, and geographical position. (a) Ship's position: latitude (blue) and longitude (green). (b) Ozone mixing ratio at port side (blue) and starboard side (green), with difference between the two instruments (red). The black dots denote for 5-min intervals when the difference between the two O_3 sensors is more than 3 ppb. (c) Data at 5-min intervals of relative wind velocities (u_X (red), u_Y (green), and $|u|$ (blue)) measured at the altitude of the light path. Negative u_X corresponds to wind from the bow; negative u_Y corresponds to wind from the starboard side. The black dots indicate 5-min intervals when u_X was less than −2 m/s or $|u|$ did not exceed 7 m/s. (d) Data at 20-min intervals of NO (blue) and NO_X (red) mixing ratios. The black dots indicate when NO_X exceeds 15 ppt. (e) CO mixing ratio. (f) 1-σ statistical error of the OH DOAS measurement (in cm^{-3}). (g) OH DOAS data. Measurements which fall into a time interval which were indicated by the selection of ozone difference, wind speeds, and NO_X mixing ratio are black. The remaining, unpolluted data have blue symbols.

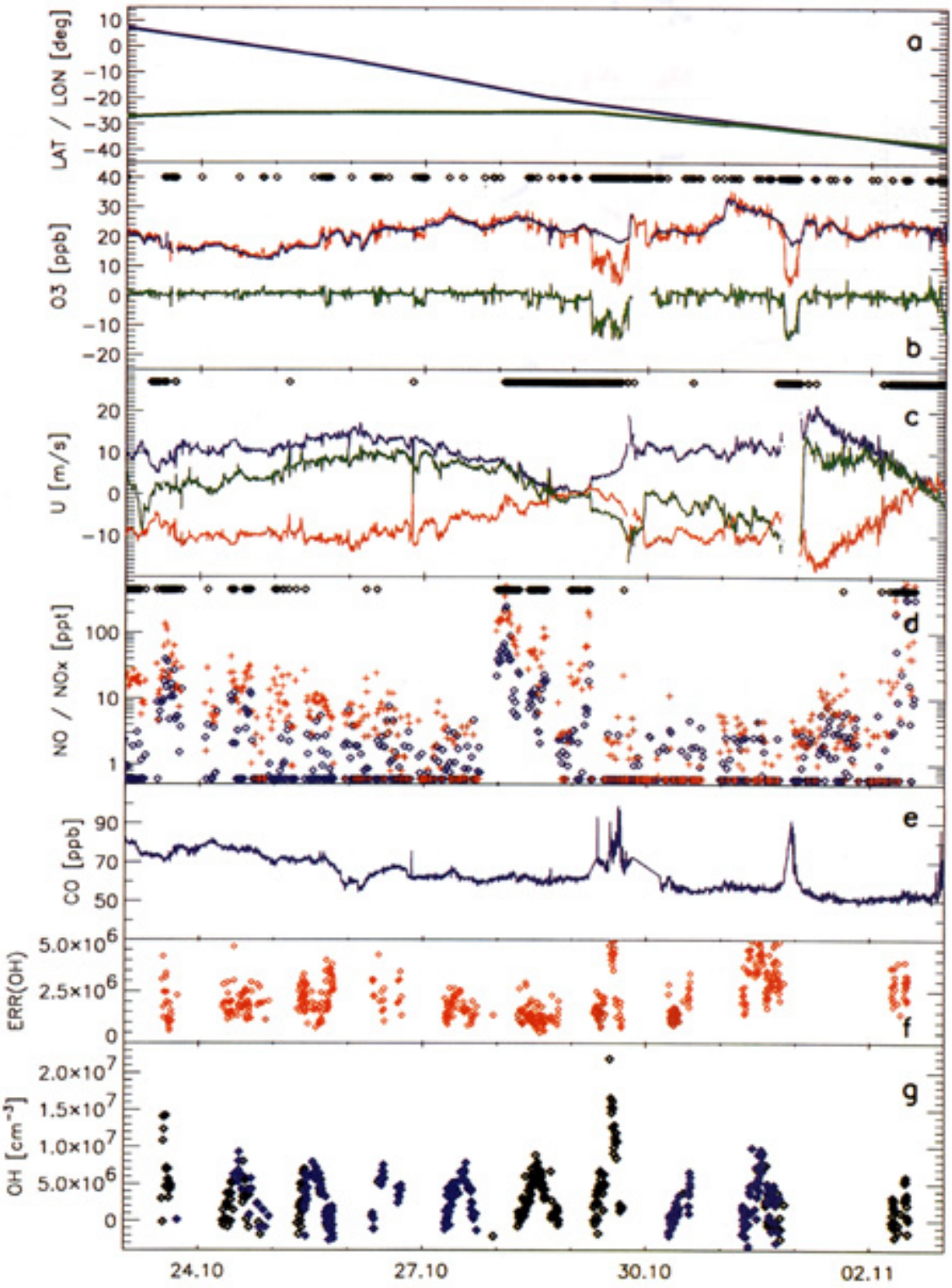
LAT / LON [deg]
10
0
−10
−20
−30
−40
a
O3 [ppb]
40
30
20
10
0
−10
−20
b
U [m/s]
20
10
0
−10
c
NO / NOx [ppt]
100
10
1
d
CO [ppb]
90
70
50
e
ERR(OH)
5.0×10^6
2.5×10^6
0
f
OH [cm^-3]
2.0×10^7
1.5×10^7
1.0×10^7
5.0×10^6
0
g
24.10
27.10
30.10
02.11

Plate 1.

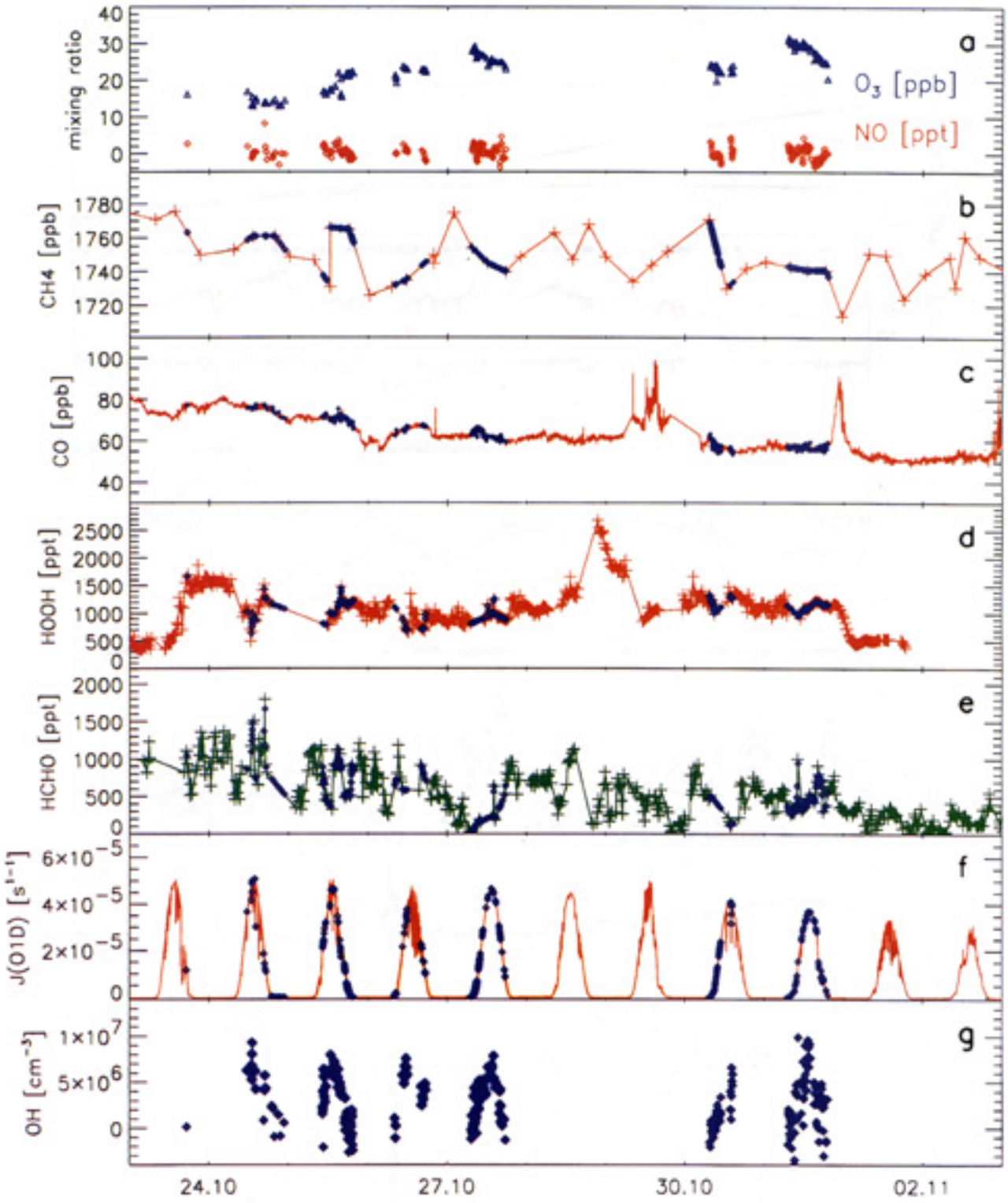

Plate 2. Measured time series of OH concentration and its precursors showing the values of the precursors interpolated or averaged at the time of the OH measurements. From top to bottom: (a) NO (red) [*Weller et al.*, 2000] and ozone (blue) at those times where OH measurements are available (b) Methane mixing ratio as measured (red) (Gautrois et al., unpublished data) and interpolated (blue). (c) CO mixing ratios as measured (red) (Gautrois et al., unpublished data) and interpolated (blue). (d) H_2O_2 mixing ratios as measured (red) [*Weller et al.*, 2000] and interpolated (blue). (e) HCHO mixing ratios as measured (green) [*Weller et al.*, 2000] and interpolated (blue). (f) Ozone photolysis frequency $J(O^1D)$ as measured (red) and averaged (blue). (g) OH DOAS data. Only selected data for clean air conditions, see Plate 1 for details.

and horizontal relative wind speed $|u|$ yield important indications for the data selection. Until October 28 the positive u_Y component and the highly negative u_X component indicate the southeasterly trade wind region, while from October 29 to October 31 westerly components prevailed. The transition between these periods is characterized by low relative wind speeds. The small u_X component means that the absolute wind had a strong northerly component of the order of the ship's speed of 12 knots (6 m/s). As is indicated in Plate 1 (black diamonds), we excluded all measurements from further analysis where the relative wind was below 7 m/s or the wind component from the bow was below 2 m/s ($u_X > -2$ m/s).

The vertical component u_z (not shown) of the relative wind is strongly correlated with the relative wind speed $|u|$ ($r = 0.82$) and the u_X component ($r = -0.80$). The ratio $u_z/|u|$ of ≈ 0.3 indicates a strong updraft encountered on the first few meters of the compass deck where the DOAS light path was located which might reduce the effective sampling height over the ocean. Since the other trace gases were sampled from the compass deck at about the same altitude (±3 m), their sampling height would have been reduced accordingly.

A second pollution indicator was the mixing ratio of CO which was measured 5 m off the port side every 5 min. The CO levels smoothly decrease from 80 ppb in the northern hemisphere to 50 ppb at 40°S. However, some sharp peaks, i.e., on October 29 and October 31, indicate events of local pollution. The peaks occur during times of low wind speed when the wind came from the starboard side ($u_Y < 0$; see Figure 1). The CO observation thus supports the previous selection based on the wind speed data.

Another sensitive parameter for local pollution is NO_X. The NO_X levels during the OH measurement period varied between 300 ppt and below the 2-σ detection limit of 6 ppt (Plate 1). The NO_X mixing ratios decrease from October 23 to the October 27 from peak levels of 100 ppt to values below 10 ppt. The scatter in the range below 10 ppt is caused by the fact that these measurements were carried out close to the detection limit of a single 20-min data point. Since the aim of this campaign was the observation of OH in clean air, we introduced an upper limit of 15 ppt of NO_X for the selection of the proper OH data. Higher values of NO_X are marked by black symbols in Plate 1, indicating the possible influence of ship pollution or continental influence.

Finally, we analyzed the ozone mixing ratio recorded at two different locations of the ship (Figure 3). The ozone readings of both instruments clearly follow each other for most of the observation period. However, at some occasions we observed a significant difference between the sensors. The major differences occur simultaneously with the spikes in CO on October 29, October 31, and November 2. These drops in ozone on one sensor are most likely caused by titration with NO advected from the ship's exhaust. These situations also coincide with low relative wind speeds. However, we also observed smaller differences for shorter time periods, often only for one 5-min interval. We also marked these intervals as questionable, since it is not clear what causes the disturbance of one of the sensors. Since the wind was blowing from the bow in these cases, electronic problems could also have occurred.

After the identification of time periods with obvious or possible pollution by the ship and its exhaust, we split the OH data set into two groups: The polluted group contains OH data if part of the DOAS integration interval fell into one of the 5-min intervals which were marked as possibly polluted. The remaining data set of 238 points is considered as not influenced by the ship's exhaust. The polluted data covered all measurements of October 23, October 28, October 29, and November 2, while on October 24, October 25, and October 31 only part of the data were possibly influenced, as shown in the lower panel of Plate 1.

3.2. Description of Selected Data

The clean air data set of 238 DOAS measurements on 6 days covers a range from -5×10^6 cm^{-3} to 1×10^7 cm^{-3} as shown in the frequency distribution (Figure 5).The average OH concentration of 2.7×10^6 cm^{-3} is not very meaningful, since the data were not sampled regularly over the days. Also shown is the distribution of the measurement error indicating a most likely value of 1.8×10^6 cm^{-3}, which is about twice the value encountered during the POPCORN field campaign (see Figure 4 of *Brandenburger et al.* [1998]). As was mentioned in the previous section, the poorer performance of the instrument was caused by the rough experimental conditions aboard the ship.

Since the OH concentration varies during the day owing to changing photolytic production, we selected the nighttime data when OH is expected to vanish. In fact, the distribution of the nighttime OH values centers around the near-zero average of $(0.3\pm3.0)\times10^5$ cm^{-3}. The width of the distribution is consistent with the individual error, the distribution of which is also shown in Figure 5.

The frequency distributions of the concentrations and the measurement errors of SO_2, HCHO, and $C_{10}H_8$ which are simultaneously measured by the DOAS instrument indicate average concentrations far below the detection limit of an individual measurement. In the case of SO_2 and $C_{10}H_8$ also the error of the mean $(\sigma/\sqrt{238})$ is larger than the mean itself. However, in the case of formaldehyde the average concentration $(1.1\times10^{10}$ cm$^{-3})$ is significantly different from zero and corresponds almost perfectly to the average of the simultaneously measured HCHO mixing ratios of 500 ppt by *Weller et al.* [2000].

The frequency distribution of the optical density of the unknown absorber X shows a clear maximum at

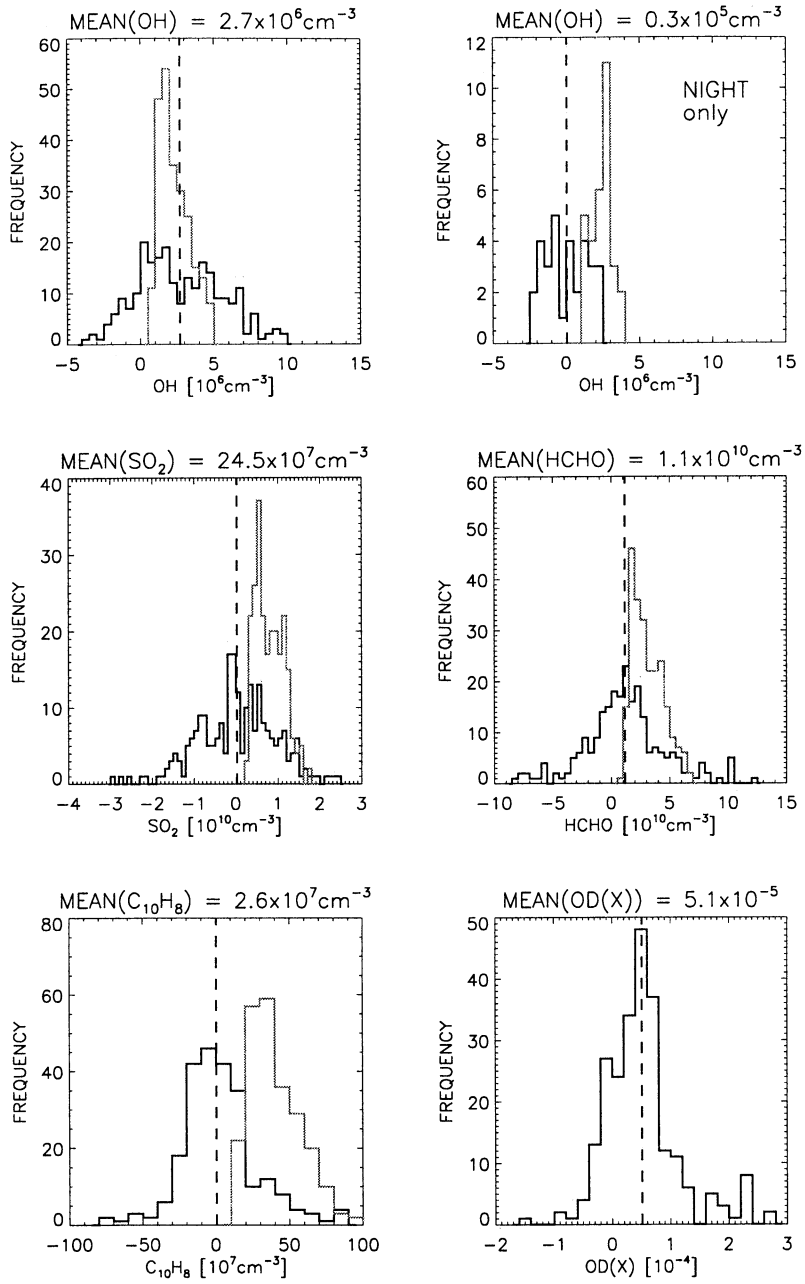

Figure 5. Frequency distributions for the concentrations (heavy solid lines) and the measurement error (light solid lines) of OH (all data and night only), SO_2, $C_{10}H_8$, and HCHO for the selected clean air data set. No error distribution is given for the optical density of the unknown absorber X, since the error of a single line is not available in the bootstrap technique described by *Hausmann et al.* [1999]. The dashed line corresponds to the mean of the respective distribution of concentrations.

5×10^{-5} which agrees with the value found during the POPCORN campaign (see Figure 2 of *Brandenburger et al.* [1998]). Similar to their findings, we did not observe any significant dependency of the optical density of X on daytime, solar radiation, or air composition. As was pointed out by *Brandenburger et al.* [1998], other long-path experiments also detected this absorption line. Thus we conclude that this absorption feature is most likely related to a ubiquitous air constituent.

Plate 2 shows the selected OH data set with the simultaneous measurements of O_3, NO, CH_4, CO, H_2O_2, HCHO, and $J(O^1D)$. Since the other measurements were not recorded at the time resolution of the DOAS OH instrument we applied the following procedure to calculate the respective values of the trace gases, temperature, and photolysis frequencies for each OH data point in a three-step procedure:

1. If one data point was available during the mea-

surement period of the DOAS instrument, this data point was assigned to the OH measurement.

2. If two or more data points were present, the values were averaged and assigned to the OH measurement.

3. If no data point was present, we linearly interpolated between the two nearest neighbors in time in the data set. The maximum interpolation time difference was set to 12 hours for methane, 1 hour for NO, HCHO, H_2O_2, ozone, CO, and H_2O, and 10 min for the photolysis frequencies.

For all 238 selected data points this procedure found a complete set of trace gas concentration and other parameters. As is shown in Plate 2 the CO, NO, and O_3 data for the selected data set cover the range of 54–78 ppb (mean: 63 ppb), −4 to +8 ppt (mean: 0.4 ppt), and 13–32 ppb (mean: 24 ppb), respectively. Average levels of HCHO and H_2O_2 for the restricted OH data set were 504 ± 289 ppt and 1054 ± 171 ppt, respectively [*Weller et al.*, 2000]. These values indicate that the selected measurements were recorded at baseline conditions where the formation of OH is dominated by the primary production through ozone photolysis (R1).

The selected data were recorded on 6 days:

1. October 24 was the day we crossed the equator at 1730 UTC. The ozone levels during the OH measurements were about 18 ppb, and we encountered constant CO mixing ratios of about 75 ppb. The levels of NO_X during daytime were between 10 ppt and 50 ppt, which resulted in the rejection of some data points (Plate 1). However, the wind component along the ship was from the bow with at least 5 m/s. Under these conditions, we do not expect the NO_X to be affected by pollution from the ship's exhaust. The elevated NO_X levels might be explained by sources on the African coast which is supported by back trajectory calculations (Gautrois et al., unpublished data). High wind speeds and high waves directly translated into increased pitch of the ship compared with other measurement days. Thus strong modulation in the laser light intensity occurred, leading to enlarged error bars of the OH measurements (Plate 1).

2. October 25 started with drizzle in the morning before 0800 UTC. It was characterized by ozone levels of 20 ppb and nearly constant CO of 75 ppb. The levels of NO_X were lower than those on the previous day, but most data were still in the range of 10 ppt. Back trajectories indicated decreasing influence from the continental sources. This was also supported by decreasing levels of CO, reaching 60 ppb in the afternoon. Many of the OH data in the morning and in the afternoon show unusually large error bars caused by the stormy weather conditions. The data after sunset scattered around zero within the range given by the error bars, indicating quality of the calculation of the measurement precision.

3. October 26 OH measurements were interrupted by a number of rain events. However, all data points were selected. The continuously operating instruments recorded nearly constant mixing ratios of NO_X below 10 ppt, CO at 60 ppb, and ozone at 20 ppb. The sparse OH measurements followed the curve of the $J(O^1D)$ photolysis rate (Plate 2).

4. October 27 was a clean-air day: all NO_X measurements were below the detection limit and CO was constant at 60 ppb. The ozone level was slightly decreasing during the day at a level of 25 ppb. The OH concentration followed the diurnal variation of $J(O^1D)$. Nearly no clouds were present which is demonstrated by the smooth curve of $J(O^1D)$. At local noon we encountered the minimum solar zenith of the cruise ($\chi_{min} = 0.8°$).

5. October 30 NO_X, ozone, CO, and wind velocity measurements showed ideal conditions for background photochemistry. Also, the primary production of OH was only slightly modulated by some clouds. However, only the OH data recorded in the early morning showed reasonably small error bars, and the data followed the increase of the photolysis frequency $J(O^1D)$ from 0800 to 1100. After 1100 we were faced with a number of technical problems (power surge, computer errors) which reduced the number and the quality of the data substantially.

6. October 31 NO_X, ozone, CO, and wind velocity measurement again showed ideal conditions for background photochemistry. Also, the photolysis of ozone was only slightly modulated by some clouds. However, the OH data showed large error bars which were caused by strong pitch and roll of the ship due to waves generated by a hurricane which went through the area a day before. The OH data of this day clearly showed the limitation of a delicate laser optical instrument aboard a ship under rough conditions.

3.3. Model Analysis of Selected Data

In order to interpret our experimental OH data we used a simple photochemical box model which calculates the concentrations of short-lived species like OH. Our model is based on the Facsimile solver [*AEA Technology*, 1994]. The mechanism described in Table 3 includes a simple CO and methane chemistry of the troposphere. It describes the production of OH from photolysis and its reaction with methane, H_2, and CO and the subsequent chemistry of HO_2, CH_3O_2, and formaldehyde. The model input was based on the measured concentrations of NO, HCHO, H_2O_2, CH_3O_2H, CO, O_3, and CH_4 (Plate 2), the measured photolysis frequencies of O_3, NO_2, HCHO, H_2O_2, and CH_3O_2H, and the measured meteorological parameters T, p, and relative humidity. The mixing ratio of H_2 was set to 550 ppt, and all rate constants were taken from *DeMore et al.* [1997] (except HO_2 + NO, taken from *Bohn and Zetzsch* [1997]). The radical species OH, HO_2, CH_3O_2, and NO_2 were calculated into steady state for each point of the DOAS OH measurements.

We did not include any NMHC or other volatile organic compounds (VOC) in our model calculation, since Gautrois et al., (unpublished data) found low con-

Table 3. Reactions and Reaction Rates Used for the Model Calculations.[a]

	Reaction	Rate Constant
	OH Production	
(R1)	$O_3 + h\nu \rightarrow O_2 + O(^1D)$	$J(O^1D)$
(R2)	$H_2O + O(^1D) \rightarrow 2\,OH$	2.2×10^{-10}
(R3)	$N_2 + O(^1D) \rightarrow N_2 + O(^3P)$	$1.8 \times 10^{-11} \exp(110\,K/T)$
(R4)	$O_2 + O(^1D) \rightarrow O_2 + O(^3P)$	$3.2 \times 10^{-11} \exp(70\,K/T)$
(R5)	$H_2O_2 + h\nu \rightarrow 2\,OH$	$J(H_2O_2)$
(R6)	$HO_2 + NO \rightarrow NO_2 + OH$	9.7×10^{-12}
(R7)	$HO_2 + O_3 \rightarrow 2\,O_2 + OH$	$1.1 \times 10^{-14} \exp(-500\,K/T)$
	OH Reactions	
(R8)	$CO + OH\,(+O_2) \rightarrow CO_2 + HO_2$	$1.5\times10^{-13}\,(1. + 0.6 \times P_{atm})$
(R9)	$CH_4 + OH \rightarrow CH_3O_2 + H_2O$	$2.5 \times 10^{-12} \exp(-1775\,K/T)$
(R10)	$CH_3O_2H + OH \rightarrow 0.7\,CH_3O_2 + 0.3\,(HCHO + OH)$	$3.8 \times 10^{-12} \exp(200\,K/T)$
(R11)	$H_2 + OH \rightarrow H_2O + HO_2$	$5.5 \times 10^{-12} \exp(-2000\,K/T)$
(R12)	$H_2O_2 + OH \rightarrow H_2O + HO_2$	$2.9 \times 10^{-12} \exp(-160\,K/T)$
(R13)	$HCHO + OH \rightarrow CO + H_2O + HO_2$	1.0×10^{-11}
(R14)	$O_3 + OH \rightarrow HO_2 + O_2$	$1.6 \times 10^{-12} \exp(-940/\,KT)$
(R15)	$NO_2 + OH \rightarrow HNO_3$	8.9×10^{-12}
(R16)	$HO_2 + OH \rightarrow H_2O + O_2$	$4.8\times10^{-11} \exp(250\,K/T)$
	HO_2 and RO_2 Reactions	
(R17)	$2\,HO_2 \rightarrow H_2O_2 + O_2$	$2.3\times10^{-13} \exp(600\,K/T) + 1.7\times10^{-33} \exp(1000\,K/T) \times M$
(R18)	$H_2O + 2\,HO_2 \rightarrow H_2O + H_2O_2$	$3.1\times10^{-34} \exp(2820\,K/T) + 2.7\times10^{-54} \exp(3180\,K/T) \times M$
(R19)	$CH_3O_2 + HO_2 \rightarrow CH_3O_2H + O_2$	$3.8 \times 10^{-13} \exp(800\,K/T)$
(R20)	$2\,CH_3O_2 \rightarrow 1.5\,HCHO + HO_2$	$2.5\times10^{-13} \exp(190\,K/T)$
(R21)	$CH_3O_2 + NO \rightarrow HCHO + HO_2 + NO_2$	$3.0 \times 10^{-12} \exp(280\,K/T)$
	NO_X Reactions	
(R22)	$NO + O_3 \rightarrow NO_2 + O_2$	$2.0 \times 10^{-12} \exp(-1400\,K/T)$
(R23)	$O(^3P) + O_2 \rightarrow O_3$	$6.0 \times 10^{-34} \times (T/300\,K)^{-2.3} \times M$
	Other Photolysis Reactions	
(R24)	$CH_3O_2H + h\nu \rightarrow HCHO + HO_2 + OH$	$J(CH_3O_2H)$
(R25)	$HCHO + h\nu \rightarrow CO + 2\,HO_2$	$J_R(HCHO)$
(R26)	$HCHO + h\nu \rightarrow CO + H_2$	$J_M(HCHO)$
(R27)	$NO_2 + h\nu \rightarrow NO + O(^3P)$	$J(NO_2)$

[a]All rate constants were taken from *DeMore et al.* [1997] with the exception of reaction (R6), where the value of *Bohn and Zetzsch* [1997] was used. Ambient measured temperature and pressure were used as input. The photolysis frequencies were set to the values simultaneously measured by spectroradiometry. Temperature, pressure, and humidity were taken from ambient measurements. H_2 was set to 550 ppb for all model runs.

centrations of light alkanes (ethane, 350 ppt; propane, 35 ppt; *n*-butane, 12 ppt; *n*-pentane, 11 ppt) which only marginally (always less than 2%) influence the OH levels. The corresponding OH lifetimes range from 8 min for ethane to to 23 min for *n*-butane compared to 3.3 s for the lifetime of OH due to CO at 50 ppb. We also excluded the OH reaction with dimethyl sulfide

$$OH + CH_3SCH_3 \rightarrow \text{products} \quad ,$$

since the levels of DMS measured by *Sciare et al.* [2000] during this part of the cruise never exceeded 150 ppt. The DMS levels during the OH measurements, however, were even lower (81 ± 23 ppt) with minor influence on the observed OH levels.

Figure 6 shows the result of the model calculations as correlation between the measured and modeled OH concentrations. The correlation coefficient $r = 0.721$ indicates that only $r^2 = 52\%$ of the scatter of the measured data can be explained by the model. However, a Monte Carlo ($N = 1000$) simulation which varies the single measured OH within the range given by the precision of the experimental OH yields an average correlation coefficient $r = 0.749 \pm 0.029$ which designates a 56% maximum of r^2 if we assume a perfect model and normal distribution of the experimental errors. Despite the poor correlation, we can deduce a slope from this data set. A linear regression weighted with the statistical error of the measurements and an assumed statistical error of the model calculation (10% of the model value; see next paragraph) yields an insignificant intercept of $(-0.14 \pm 0.16) \times 10^6\,cm^{-3}$ and a slope of 0.860 ± 0.044 indicating a 16% overprediction by the model. The statistical parameters of the regression are $\chi^2 = 244$ associ-

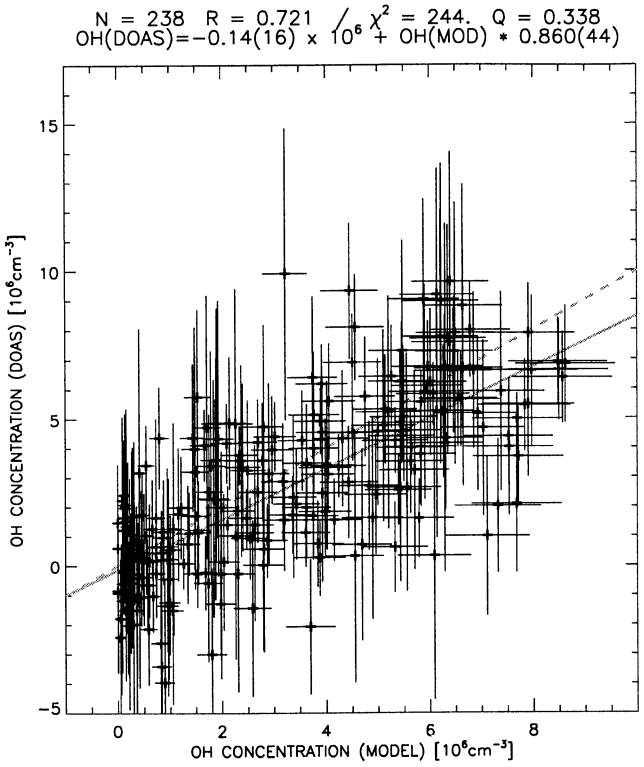

Figure 6. Correlation between the measured concentration of OH and the model. The vertical error bars denote the 1-σ precision of the measured OH concentration, and the horizontal bars show 10% model error. The dashed line corresponds to 1:1, while the solid line represents the regression given in the parameters set at the top of this figure. See text for the discussion of regression parameters.

ated with a goodness-of-fit probability $Q = 0.34$. Thus the assumption of a linear relationship between measurement and model agrees with observed values and errors. The scatter around the regression line can be explained by the measurement errors of OH alone even if we consider a small (15%) overestimation of our measurement errors as discussed by *Hausmann et al.* [1999].

The 16% discrepancy between model and measurement is not likely to be explained by the systematic error of our experimental data, since the error of the OH absorption cross section is about 6%, as was discussed in the experiment section. A major uncertainty of the regression analysis above is the assumption of the model error. We repeated the regression at 0%, 20%, and 30% model error which gives a span in the slope from 0.82 to 1.01, as shown in Table 4. Consequently, a 30% statistical error would provide a perfect match between OH measurements and model. However, on the basis of the model analysis of former OH field campaigns, we took an model error of 10% as the most likely value. Beyond the model error, other factors like the accuracy of measured input parameters used in the model are likely to influence the regression's slope.

A critical point when analyzing the correlation between measured and modeled OH could be the influence of the interpolation or averaging of the model input data. In order to test this effect, five new model runs were performed with the interpolated or averaged NO, HCHO, H_2O_2, CO, and $J(O^1D)$ values replaced by their nearest measured data points. The slopes were found in the range between 0.855 (NO) and 0.861 ($J(O^1D)$), indicating a minor contribution to the uncertainty of the model.

A major contribution to the model values is the photolysis frequency of ozone, $J(O^1D)$. Its measurements were subject to extensive investigation during recent years. Figure 7 shows a linear dependence of OH with $J(O^1D)$ for the measured ($r = 0.75$) and the modeled ($r = 0.96$) data set. The slope of a weighted linear fit is $(1.37 \pm 0.07) \times 10^{11}$ cm^{-3}s and $(1.59 \pm 0.01) \times 10^{11}$ cm^{-3}s for the measured and modeled data, respectively. Consequently, to match measured and modeled OH values by the adaptation of the ozone photolysis frequencies, it had to be reduced by 14%, which is in the range of the possible systematic error of the spectroradiometer measurements [*Hofzumahaus et al.*, 1999]. The same slope is also calculated if a subset of the selected data where the errors of the OH measurements were less than 1.74×10^6 cm^{-3} is examined (Figure 7). The cutoff corresponds to twice the average error of the OH measurements during the POPCORN field campaign in 1994. In this case, the correlation coefficient for the measured data increases from 0.75 to 0.85, whereas the

Table 4. Dependence of the Slope of the Regression OH Measured Versus Model on the Assumed Statistical Model Error and the Model Input Parameters HCHO, H_2O_2, O_3, CO, NO, and Photolysis Frequencies.

Parameter	Variation	Slope
model error	0%	0.82(4)
	10% [a]	0.86(4) [a]
	20%	0.94(5)
	30%	1.01(6)
H_2O_2	+30%	0.85(4)
	−30%	0.86(4)
HCHO	+30%	0.88(5)
	−30%	0.84(4)
CO	+12%	0.90(5)
	−12%	0.83(4)
O_3	+5%	0.82(4)
	−5%	0.90(5)
$J(O^1D)$	+15%	0.77(4)
	−15%	0.98(5)
all J	+15%	0.76(4)
	−15%	1.00(5)
NO	−100%	0.89(5)
	+100%	0.83(5)
	= 5 ppt	0.81(5)
	= 10 ppt	0.75(4)

[a] Corresponds to the regression line drawn in Figure 6.

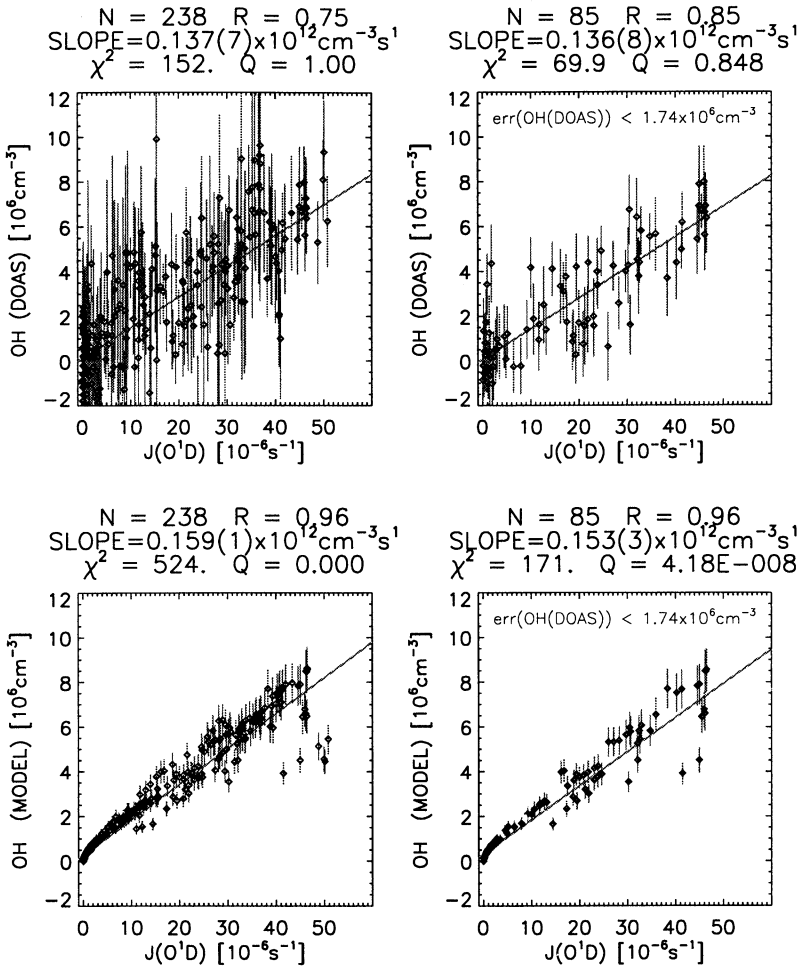

Figure 7. Correlation between the concentration of OH and the measured photolysis frequency of ozone $J(O^1D)$. (top left) All measured DOAS OH concentrations, the error bars correspond to the 1-σ error. (bottom left) Model OH for the same data set. For the weighted linear regression the errors were assumed to be 10% of the calculated value. (top right) selected OH data with a 1-σ precision of less than $1.78\times10^6\,cm^{-3}$ (see text). (bottom right) Model OH for the error selected data set.

slope is not changed, indicating that the larger scatter of the the less precise data points do not influence the ratio of OH and $J(O^1D)$. *Ehhalt and Rohrer* [2000] performed a correlation between OH and $J(O^1D)$ for the data of the POPCORN campaign. Their slope of $(3.94\pm0.04)\times10^{11}\,cm^{-3}s$ indicates that under rural conditions (at an average NO mixing ratio of 440 ppt) the OH yield per photolyzed ozone molecules nearly triples in comparison with the low NO conditions observed here. The sensitivity of the model slope on the photolysis rate measurements is given in Table 4. If $J(O^1D)$ or all photolysis frequencies were reduced by 15%, the slope would be unity within the error range. The high sensitivity on $J(O^1D)$ demand high-accuracy photolysis frequency measurements for the modeling of tropospheric OH.

The large variability of the measured NO mixing ratios below 8 ppt reflects, at least partly, the detection limit of the NO sensor. Therefore we tested the slope of the regression line with respect to four different scenarios (Table 4): no NO, double NO, NO constant at 5 ppt, and NO constant at 10 ppt. The first three runs give results for the slope within the range of the error of the original value. Setting NO to 10 ppt in the model significantly increases the model values. However, there is no evidence for high NO mixing ratios during the entire OH measurement period. In addition, higher NO concentrations increase the difference between model and measurement.

The measured concentration of OH could significantly be reduced if undetected VOCs would be present at elevated concentrations. A single-point pollution source aboard the ship would not reduce the OH level by a constant factor, since relative wind changed during the measurements, but we did not see clearly defined spikes in OH after selection of the data. Also, at about 5 m/s relative wind from the bow the travel time for an air parcel from the bow to the compass deck is only 8 s

which excludes transport from the ship's surface to the measurement height of 4 m above the deck, since the vertical wind component was only 30% of the horizontal wind. However, if the airflow was more complex, resulting in a longer travel time in the vicinity of the ship, then the ship and its evaporation might influence the local OH concentration. This topic is planned for study in the future by using a model of R/V *Polarstern* in a wind tunnel experiment.

Another uncertainty is associated with the influence of HCHO on the modeled OH concentration. The mixing ratios of HCHO encountered during this part of the cruise were relatively high, as was discussed by *Weller et al.* [2000]. Under low NO_X conditions such as those encountered here, HCHO is mainly a sink for OH. Consequently, if the measured HCHO mixing ratios were too high, the model OH values were too low. Thus lower HCHO mixing ratios would additionally increase the difference between measured and modeled values. Anyway, under the conditions encountered here the sensitivity on HCHO is small. Even a ±30% change in HCHO would alter the slope of the regression line in Figure 6 by only ±3% (Table 4). Other model parameters are of similar small influence. Typical measurement accuracies of O_3, CO, and H_2O_2 as shown in Table 4 do not substantially modify the slope of the regression. However, it should be noted, that the sensitivity of OH on O_3 is as high as 0.82 under the low NO_X conditions.

Finally, a possible sink for OH radicals is heterogeneous reactions on aerosol surfaces. *Frost et al.* [1999] measured OH during the ACE 1 campaign at various altitudes in the higher marine troposphere in the vicinity of Tasmania. Their measurements are also lower than their model, and they relate the mismatch to heterogeneous loss of OH and HO_2 when they flew through clouds. For the OH data presented here it is unlikely that heterogeneous HO_X loss can provide a significant contribution. In order to match the measured values for our data set an additional OH and HO_2 loss with $k_{het} = 0.2\,s^{-1}$ would be necessary. However, during all OH measurements the nephelometer reading at the same altitude as the OH measurement never exceeded $2.5\times10^{-5}\,m^{-1}$. Assuming an (average) particle size of 1 μm and unity sticking probability k_{het} would be of the order of $0.0025\,s^{-1}$, far off the required value. Even if a cloud of sea salt particles would be present at lower heights (< 5 m) above the sea surface providing an effective sink for OH radicals, the turbulent transfer velocity is too small to influence the OH measurements at the altitude of the compass deck.

4. Conclusions

This paper shows the first measurements of OH in the marine boundary layer above the tropical Atlantic Ocean. Despite some technical difficulties, it has been demonstrated that a complex DOAS instrument can be operated aboard a ship. We also showed that the technical problems translated into larger error bars than we expected from previous field studies.

We found a linear relationship between the measured and modeled OH concentrations with 17% higher model values. The discrepancy is clearly within the range of the combined systematic errors of $J(O^1D)$, CO, and the measured OH. The sensitivity analysis showed that the accuracy of ozone, formaldehyde, and hydroperoxide are of minor influence on the agreement between OH measurement and model. In a forthcoming paper we will also analyze the data and the model with respect to the OH and HO_2 data recorded by the Laser Induced Fluorescence instrument.

Acknowledgments. We are grateful to the *Polarstern* crew and the Logistic department of the Alfred-Wegener-Institut in Bremerhaven. We also thank Franz Rohrer for cooperation with the model and Andreas Hofzumahaus for help with the spectroradiometer. This work was supported by the European Commission under grant ENV4-CT95-0004 (Marathon project).

References

AEA Technology, Facsimile release 3.05 (user guide/technical reference), technical report, Harwell, Didcot, United Kingdom, 1994.

Armerding, W., M. Spiekermann, R. Grigonis, J. Walter, A. Herbert, and F. J. Comes, Fast scanning laser DOAS for local monitoring of trace gases, in particular tropospheric OH radicals, *Ber. Bunsen Ges. Phys. Chem.*, *96*, 314–318, 1992.

Armerding, W., et al., Testing the daytime oxidizing capacity of the troposphere: 1994 OH field campaign at the Izana Observatory, Tenerife, *J. Geophys. Res.*, *102*, 10,603–10,611, 1997.

Bister, A., Anwendung von Fouriermethoden in der Laser-Langweg Absorsorptionsspektrokopie, Diploma Thesis, Univ. of Bonn, Bonn, Germany, 1997.

Bohn, B., and C. Zetzsch, Rate constants of HO_2 + NO covering atmospheric conditions, 1, HO_2 formed by OH + H_2O_2, *J. Phys. Chem.*, *101*, 1488–1493, 1997.

Brandenburger, U., T. Brauers, H.-P. Dorn, M. Hausmann, and D. Ehhalt, In-situ measurement of tropospheric hydroxyl radicals by folded laser long-path absorption during the field campaign POPCORN in 1994, *J. Atmos. Chem.*, *31*, 181–204, 1998.

Brauers, T., M. Hausmann, U. Brandenburger, and H.-P. Dorn, Improvement of differential optical absorption spectroscopy with a multichannel scanning technique, *Appl. Opt.*, *34*, 4472–4479, 1995.

Callies, J., Absorptionsspektroskopischer Nachweis von Hydroxyl-Radikalen in der Troposphäre, Ph.D. thesis, Univ. of Cologne, Cologne, Germany, 1988.

Cooper, D. J., Estimation of hydroxyl radical concentrations in the marine atmospheric boundary layer using a reactive atmospheric tracer, *J. Atmos. Chem.*, *25*, 97–113, 1996.

Crosley, D. R., The measurement of OH and HO_2 in the atmosphere, *J. Atmos. Sci.*, *52*, 3299–3314, 1995.

Daumont, D., J. Brion, J. Charbonnier, and J. Malicet, Ozone UV spectroscopy, I, absorption cross-sections at room temperature, *J. Atmos. Chem.*, *15*, 145–155, 1992.

DeMore, W., C. Howard, S. Sander, A. Ravishankara, D. Golden, C. Kolb, R. Hampson, M. Molina, and M. Kurylo, Chemical kinetics and photochemical data for use in stratospheric modeling, Eval. *12*, Rep. JPL 97-4, Jet Propul. Lab., Pasadena, Calif., 1997.

Dorn, H.-P., U. Brandenburger, T. Brauers, and M. Hausmann, A new in-situ laser long-path absorption instrument for the measurement of tropospheric OH radicals, *J. Atmos. Sci.*, *52*, 3373–3380, 1995.

Dorn, H.-P., R. Neuroth, and A. Hofzumahaus, Investigation of OH absorption cross sections of rotational transitions in the $A_2(\Sigma)$, $\nu' = 0 \leftarrow X_2(\Pi)$, $\nu'' = 0$ band under atmospheric conditions: Implications for tropospheric long-path absorption measurements, *J. Geophys. Res.*, *100*, 7397–7409, 1995.

Ehhalt, D., and F. Rohrer, The dependence of the OH concentration on solar UV, *J. Geophys. Res.*, *105*, 3565–3571, 2000.

Ehhalt, D., H.-P. Dorn, and D. Poppe, The chemistry of the hydroxyl radical in the troposphere, *Proc. R. Soc. Edinburgh Sect. B Biol. Sci.*, *97*, 17–34, 1991.

Eisele, F. L., G. H. Mount, F. C. Fehsenfeld, J. Harder, E. Marovich, D. D. Parrish, J. Roberts, M. Trainer, and D. Tanner, Intercomparison of tropospheric OH and ancillary trace gas measurements at Fritz Peak Observatory, Colorado, *J. Geophys. Res.*, *99*, 18,605–18,626, 1994.

Frost, G. J., et al., Photochemical modeling of OH levels during the First Aerosol Characterization Experiment (ACE 1), *J. Geophys. Res.*, *104*, 16,041–16,052, 1999.

Gerlach, R., Aufbau und Charakterisierung eines Vielfachreflexionssystems zur Messung von Hydroxyl-Radikalen in der Troposphäre, Ph.D. thesis, Univ. of Cologne, Cologne, Germany, 1991.

Hausmann, M., U. Brandenburger, T. Brauers, and H.-P. Dorn, Detection of tropospheric OH radicals by long-path differential-optical absorption spectroscopy: experimental setup, accuracy, and precision, *J. Geophys. Res.*, *102*, 16,011–16,022, 1997.

Hausmann, M., U. Brandenburger, T. Brauers, and H.-P. Dorn, Simple Monte Carlo method to estimate the spectra evaluation error in differential optical absorption spectroscopy, *Appl. Opt.*, *38*, 462–475, 1999.

Hofzumahaus, A., A. Kraus, and M. Müller, Solar actinic flux spectroradiometry: A new technique to measure photolysis frequencies in the atmosphere, *Appl. Opt.*, *38*, 4443–4460, 1999.

Holland, F., U. Aschmutat, M. Heßling, A. Hofzumahaus, and D. H. Ehhalt, Highly time resolved measurements of OH during POPCORN using laser-induced fluorescence spectroscopy, *J. Atmos. Chem.*, *31*, 205–225, 1998.

Hübler, G., D. Perner, U. Platt, A. Toennissen, and D. H. Ehhalt, Ground level OH radical concentration: New measurements by optical absorption, *J. Geophys. Res.*, *89*, 1309–1319, 1984.

Kraus, A., and A. Hofzumahaus, Field measurements of atmospheric photolysis frequencies for O_3, NO_2, HCHO, CH_3CHO, H_2O_2 and HONO by UV spectroradiometry, *J. Atmos. Chem.*, *31*, 161–180, 1998.

Logan, J. A., M. J. Prather, S. C. Wofsy, and M. B. McElroy, Tropospheric chemistry: A global perspective, *J. Geophys. Res.*, *86*, 7210–7254, 1981.

McKeen, S. A., et al., Photochemical modeling of hydroxyl and its relationship to other species during the tropospheric OH photochemistry experiment, *J. Geophys. Res.*, *102*, 6467–6493, 1997.

Merienne, M. F., A. Jenouvrier, and B. Coquart, The NO_2 absorption spectrum, 1, Absorption cross-sections at ambient temperature in the 300-500 nm region, *J. Atmos. Chem.*, *20*, 281–297, 1995.

Mount, G. H., J. W. Brault, P. V. Johnston, E. Marovich, R. O. Jakoubek, C. J. Volpe, J. Harder, and J. Olson, Measurement of tropospheric OH by long-path laser absorption at Fritz Peak Observatory, Colorado, during the OH Photochemistry Experiment, fall 1993, *J. Geophys. Res.*, *102*, 6393–6413, 1997a.

Mount, G. H., F. L. Eisele, D. J. Tanner, J. W. Brault, P. V. Johnston, J. W. Harder, E. J. Williams, A. Fried, and R. Shetter, An intercomparison of spectroscopic laser long-path and ion- assisted in situ measurements of hydroxyl concentrations during the Tropospheric OH Photochemistry Experiment, fall 1993, *J. Geophys. Res.*, *102*, 6437–6455, 1997b.

Perner, D., D. H. Ehhalt, H. W. Paetz, U. Platt, E. P. Roeth, and A. Volz, OH-radicals in the lower troposphere, *Geophys. Res. Lett.*, *3*, 466–468, 1976.

Platt, U., M. Rateike, W. Junkermann, J. Rudolph, and D. H. Ehhalt, New tropospheric OH measurements, *J. Geophys. Res.*, *93*, 5159–5166, 1988.

Platt, U., J. Rudolph, T. Brauers, and G. W. Harris, Atmospheric measurements during *polarstern* cruise ANT-VII/1, 54N to 32S - An overview, *J. Atmos. Chem.*, *15*, 203–214, 1992.

Poppe, D., et al., A comparison of measured OH concentrations with model calculations, *J. Geophys. Res.*, *99*, 16,633–16,642, 1994.

Sciare, J., E. Baboukas, M. Kanakidou, U. Krischke, S. Belviso, H. Bardouki, and N. Mihalopoulos, Spatial and temporal variability of atmopheric sulfur-containing gases and particles during the ALBATROSS campaign, *J. Geophys. Res.*, *105*, 14,433–14,448, 2000.

Talukdar, R. K., C. Longfellow, M. K. Gilles, and A. R. Ravishankara, Quantum yield of $O(^1D)$ in the photolysis of ozone between 289 and 329 nm as a function of temperature, *Geophys. Res. Lett.*, *25*, 143–146, 1998.

Tanner, D. J., A. Jefferson, and F. L. Eisele, Selected ion chemical ionization mass spectrometric measurement of OH, *J. Geophys. Res.*, *102*, 6415–6425, 1997.

Thompson, A. M., The oxidizing capacity of the Earth's atmosphere: Probable past and future changes, *Science*, *256*, 1157–1165, 1992.

Thompson, A. M., et al., Ozone observations and a model of marine boundary layer photochemistry during SAGA 3, *J. Geophys. Res.*, *98*, 16,955–16,968, 1993.

Vaghjiani, G. L., and A. R. Ravishankara, Absorption cross section of CH_3OOH, H_2O_2, and D_2O_2 vapors between 210 and 365 nm at 297 K, *J. Geophys. Res.*, *94*, 3487–3492, 1989.

Weller, R., O. Schrems, A. Boddenberg, S. Gaeb, and M. Gautrois, Meridional distribution of hydroperoxides and formaldehyde in the marine boundary layer of the Atlantic (48°N-35°S) measured during the ALBATROSS campaign, *J. Geophys. Res.*, *105*, 14,401–14,412, 2000.

T. Brauers and H.-P. Dorn, Institut für Atmosphärische Chemie, Forschungszentrum Jülich, 52425 Jülich, Germany. (th.brauers@fz-juelich.de; h.p.dorn@fz-juelich.de)

M. Hausmann, Hoffmann Meßtechnik , Am Tairnbacher Weg 5, 69234 Dielheim, Germany. (hausmann@hmm.de)

A. Bister, Rational Software, Wanheimer Str. 43, 40472 Düsseldorf, Germany. (abister@rational.com)

A. Kraus, Grünenthal GmbH, Zieglerstr. 6, 52078 Aachen, Germany. (Alexander.Kraus@grunenthal.de)

(Received August 4, 2000; revised September 30, 2000; accepted October 16, 2000.)